

# Spin-flip Scattering at Chiral Interface of Helical Chains

Keita Matsubara and Kazumasa Hattori

*Department of physics, Tokyo Metropolitan University, 1-1 Minami-Osawa, Hachioji, Tokyo 192-0397, Japan*

We investigate spin-flip scattering processes of electrons when they pass a chiral interface, which is the boundary between right- and left-handed one-dimensional chain. We construct a minimal  $p$ -orbital model consisting of the right- and left-handed one-dimensional threefold helical chains connected at  $z = 0$  with the nearest neighbor hopping and the spin-orbit coupling. The dynamics of spin-polarized wave packet passing through the interface, the Green's functions, and electronic states near the interface are analyzed numerically. We find that the microscopic structure of the interface is important and this strongly affects the local electronic orbital state. This in addition to the spin-orbit coupling determines whether the spin flip occurs or not at the chiral interface and suggests a possible spin transport control by the orbital configuration at the chiral interface.

KEYWORDS: chiral crystal, interface, spin flip

## 1. Introduction

Chiral crystals lack mirror and space inversion symmetries and possess the two types of structures distinguished by handedness or chirality.<sup>1)</sup> The two structures are the mirror images with each other and called right-handed (RH) and left-handed (LH). In recent years, physics in chiral crystals have attracted great attention due to their unique properties.<sup>2)</sup> For example, the absence of the mirror and the space inversion symmetry leads to cross-correlated responses<sup>3)</sup> such as Edelstein effect<sup>4,5)</sup> and electrorotation effects.<sup>6)</sup> Phonons in chiral crystals, chiral phonons,<sup>7-9)</sup> have their own angular momenta locked by the direction of their momentum and it is known that their dispersions show the band splitting for different angular momenta.<sup>10,11)</sup> The angular momentum of phonons gives correction to the Einstein-de-Haas effect<sup>12)</sup> and it can also couple with other quantities such as electrons' spin.<sup>13,14)</sup>

Among various phenomena related to the chirality, spin-dependent and/or non-reciprocal spin transports are the key to the deeper understanding of the physics behind the chirality degree of freedom. Anisotropic transports in chiral materials such as carbon nanotubes<sup>15)</sup> and in chiral magnets<sup>17,18)</sup> have been actively studied over the past two decades. Moreover, spin selective transports in chiral molecules called chirality-induced spin selectivity (CISS), finite spin polarizations of electrons passing through chiral materials, have also been extensively studied.<sup>19,20)</sup>

To realize the “full” responses characteristic to the chirality in the chiral systems, controlling their domains is crucially important. So far, there is no established method to selectively synthesize mono chiral domain for general chiral materials. Recent studies on the basis of multipole theory<sup>6,21,22)</sup> show the importance of electric toroidal monopole in chirality enantioselection. At the boundary between the LH and RH crystals, unique interface is formed and we call it chiral interface (CIF). Such CIFs inevitably exist in chiral crystals, and thus, one can regard them as microscopic chirality “junctions” in bulk systems. In chiral magnets, such structures lead to large magnetoresistance<sup>23)</sup> and investigated theoretically.<sup>24,25)</sup> Spin-dependent phenomena in magnetic junction systems such as the tunneling magnetoresistance<sup>26)</sup> and the spin-to-charge conversion<sup>27)</sup> have also attracted great atten-

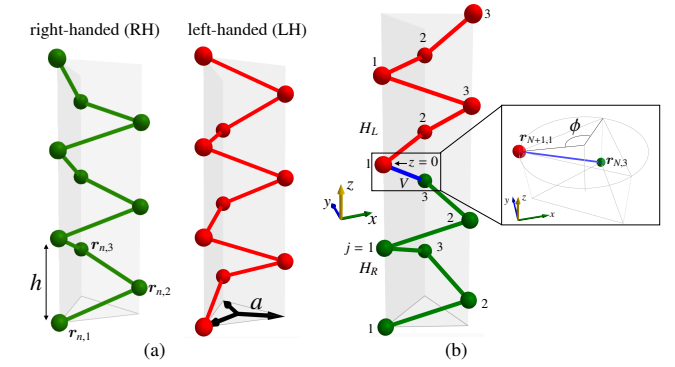


**Fig. 1.** (a) The right-handed (RH; green) and left-handed (LH; red) chain. Each unit cell contains three sublattices indexed as  $r_{n,j}$  ( $j = 1, 2, 3$ ). (b) One-dimensional chiral chain with the CIF. The blue line represents the inter-chain bond. The inset shows the parameter  $\phi$ .

tion and play one of primal roles in recent nanotechnological developments. The focused-ion beam technology<sup>28)</sup> also allows one to observe a single domain wall (if it exists) dynamics and anisotropic transport in artificially constructed structure. In this respect, it is highly important to understand the spin transport physics at these CIFs.

In this paper, we investigate how the CIF between RH and LH systems affects the spin polarization of electron passing through the CIF in chiral crystals. We analyze a minimal one-dimensional  $p$ -orbital tight-binding model with RH and LH three-fold helices connected at the origin ( $z = 0$ ). See Fig. 1. We clarify the dynamics of a spin-polarized electron wave packet passing through the CIF and the mechanism of spin-flip processes at the CIF.

This paper is organized as follows. We will introduce our model Hamiltonian in Sec. 2 and introduce our methods used in the analysis in Sec. 3. In Sec. 4, we will show the numerical results of CIF scattering and analyze the spin-flip processes at the CIF. Section 5 is devoted to the discussion about the mechanism of the spin flip at the CIF, focusing on the localized modes at the CIF and their orbital character. Finally, we summarize the results of this paper in Sec. 6.

## 2. Model

In this section, we provide our model Hamiltonian. We consider a one-dimensional three-fold helical chain with a CIF at its center. Such a three-fold helical structure can be found e.g., in Tellurium.<sup>5)</sup> Our model is a simplified one taking a single helical chain in the Te-like crystal structure, and one of minimal models for analyzing the electron scattering at the CIF.

### 2.1 Model Hamiltonian

The system we will analyze in this paper consists of two three-fold helical chains along the  $z$ -direction with different handedness as shown in Fig. 1(a) and we connect them at  $z = 0$ . This generates a CIF [Fig. 1(b)]. We assume that the half chain for  $z < 0$  is the RH one and label the site position  $\mathbf{r}_{n,j} = (-a \cos \theta_j, -a \sin \theta_j, z_{n,j})$  with  $\theta_j = \frac{2\pi}{3}(j-1)$  and  $z_{n,j} = h[n - N - 1 + \frac{h}{3}(j-1)]$ . Here,  $n$  ( $= 1, 2, \dots, N$ ) is the index for the unit cell in the RH chain and  $j$  ( $= 1, 2, 3$ ) is that for the sublattice. Similarly, the  $z \geq 0$  part is the LH one with the site position  $\mathbf{r}_{n,j} = [-a \cos(\theta_{j+1} - \phi), a \sin(\theta_{j+1} - \phi), z_{n,j}]$  for  $n = N+1, N+2, \dots, 2N$ , where we introduce the parameter  $\phi$  as shown in the inset of Fig. 1(b). This determines the structure of the CIF at  $z = z_{\text{CIF}} \equiv (z_{N,3} + z_{N+1,1})/2$ . Hereafter, we set  $a = 1$  and  $h = 1$ .

Next, we explain the Hamiltonian used in this study. To discuss the correlation between the chirality and spins, one needs to consider the spin-orbit coupling (SOC). One of the minimal setting is a  $p$ -electron system with three  $p_x, p_y$  and  $p_z$  orbitals since they have finite SOC. The orbital degrees of freedom can take into account the effects of helical structure. We use a vector form  $\hat{\mathbf{p}}_{n,j,\sigma}^\dagger = (\hat{p}_{n,j,x,\sigma}^\dagger, \hat{p}_{n,j,y,\sigma}^\dagger, \hat{p}_{n,j,z,\sigma}^\dagger)$ , where  $\hat{p}_{n,j,\ell,\sigma}^\dagger$  is the creation operator of  $p_\ell$  ( $\ell = x, y, z$ ) electron at  $\mathbf{r}_{n,j}$  with the spin  $\sigma$  ( $= \uparrow, \downarrow$ ). For simplicity, we have ignored the orbital dependent local crystal field. Hamiltonian consists of the intra-chain part  $\hat{H}_{R,L}$  and the inter-chain part  $\hat{V}$  as  $\hat{H} = \hat{H}_R + \hat{H}_L + \hat{V}$  with

$$\hat{H}_{R(L)} = \sum_{n,i,\sigma}^{1 \leq n \leq N}^{(N+1 \leq n \leq 2N)} (\hat{\mathbf{p}}_{n,j+1,\sigma}^\dagger \cdot \mathbf{d}_{j,j+1}^n) (\hat{\mathbf{p}}_{n,j,\sigma} \cdot \mathbf{d}_{j,j+1}^n) + \text{h.c.} \\ + \lambda \sum_{n,j,\ell,\ell',\sigma,\sigma'}^{1 \leq n \leq N}^{(N+1 \leq n \leq 2N)} \hat{p}_{n,j,\ell,\sigma}^\dagger (\mathbf{L} \cdot \mathbf{S})_{p_{\ell,\sigma}, p_{\ell',\sigma'}} \hat{p}_{n,j,\ell',\sigma'}, \quad (1)$$

$$\hat{V} = \hat{V}_{LR} + \hat{V}_{RL}, \quad (2)$$

$$\hat{V}_{LR} = \sum_{\sigma} (\hat{\mathbf{p}}_{N+1,1,\sigma}^\dagger \cdot \mathbf{d}_{\text{CIF}}) (\hat{\mathbf{p}}_{N,3,\sigma} \cdot \mathbf{d}_{\text{CIF}}) = \hat{V}_{RL}^\dagger. \quad (3)$$

Here, the first term in the RHS of  $\hat{H}_{R,L}$  describes the nearest neighbor (NN) hopping and the second one does the SOC with the coupling constant  $\lambda$ .  $\hat{V}_{LR(RL)}$  in Eq. (3) represents the hopping from RH (LH) to the LH (RH) chain at the CIF. We have set the NN hopping to 1 as a unit of energy and  $\mathbf{d}_{j,j+1}^n = (\mathbf{r}_{n,j+1} - \mathbf{r}_{n,j})/|\mathbf{r}_{n,j+1} - \mathbf{r}_{n,j}|$ , where  $\mathbf{r}_{n,4}$  should be regarded as  $\mathbf{r}_{n+1,1}$ . We take into account only the  $\sigma$ -bond<sup>29)</sup> for the NN hoppings, and thus, the electrons in the orbitals along the bond direction  $\mathbf{d}_{j,j+1}^n$  can hop, while the others cannot.  $\mathbf{d}_{\text{CIF}} = (\mathbf{r}_{N+1,1} - \mathbf{r}_{N,3})/|\mathbf{r}_{N+1,1} - \mathbf{r}_{N,3}|$  is the bond direction at the CIF and depends on  $\phi$ . Although variations in  $\phi$  cause changes in the bond length, we set the absolute value of the hopping unchanged. This is because it is not important in comparison

to the change in the direction.  $(\mathbf{L} \cdot \mathbf{S})_{p_{\ell,\sigma}, p_{\ell',\sigma'}}$  is the  $(p_{\ell,\sigma}, p_{\ell',\sigma'})$  component of the matrix  $\mathbf{L} \cdot \mathbf{S}$ . This has a form in the basis of  $\{p_{x\uparrow}, p_{x\downarrow}, p_{y\uparrow}, p_{y\downarrow}, p_{z\uparrow}, p_{z\downarrow}\}$  as

$$\mathbf{L} \cdot \mathbf{S} = \frac{1}{2} \begin{pmatrix} 0 & 0 & i & 0 & 0 & 1 \\ 0 & 0 & 0 & -i & -1 & 0 \\ -i & 0 & 0 & 0 & 0 & i \\ 0 & i & 0 & 0 & i & 0 \\ 0 & -1 & 0 & -i & 0 & 0 \\ 1 & 0 & -i & 0 & 0 & 0 \end{pmatrix}, \quad (4)$$

where  $\mathbf{L} = (L_x, L_y, L_z)$  and  $\mathbf{S} = (S_x, S_y, S_z)$  are the orbital and spin angular momentum matrix, respectively.

### 2.2 The eigenenergy and the eigenstates

$\hat{H}$  [Eqs. (1)-(3)] can be easily diagonalized numerically with the open boundary condition at  $\mathbf{r}_{1,1}$  and  $\mathbf{r}_{2N,3}$  and one obtains the eigenenergy  $\varepsilon_m$  as

$$\hat{H} = \sum_{m=1}^{36N} \varepsilon_m \hat{c}_m^\dagger \hat{c}_m. \quad (5)$$

Here,  $\hat{c}_m^\dagger$  is the creation operator of the  $m$ th eigenstate  $|m\rangle = \hat{c}_m^\dagger |0\rangle$ , where  $|0\rangle$  is the vacuum.  $\hat{c}_m^\dagger$  can be written as a linear combination of  $\hat{p}_{n,j,\ell,\sigma}^\dagger$  as

$$\hat{c}_m^\dagger = \sum_{n,j,\ell,\sigma} T_{n,j,\ell,\sigma;m} \hat{p}_{n,j,\ell,\sigma}^\dagger, \quad \hat{p}_{n,j,\ell,\sigma}^\dagger = \sum_m T_{n,j,\ell,\sigma;m}^* \hat{c}_m^\dagger, \quad (6)$$

where  $T_{n,j,\ell,\sigma;m}$  is a  $36N \times 36N$  unitary matrix. Since the time-reversal symmetry is present,  $\varepsilon_m$  is at least two-fold degenerate. Note that there is no translational symmetry and thus the wavenumbers are not good quantum numbers.

## 3. Methods

Here, we explain methods for our analyses of electron scatterings at the CIF. First, we consider a situation where a spin polarized electron is injected to the RH chain at the initial time  $t = 0$ . The wave packet diffuses as the time passes. It reaches the CIF and then is scattered. We derive an expression for the dynamics of the wave packet propagating on the filled Fermi sea in contrast to one-particle wave packet studies, for example, in mesoscopic ring devices<sup>30)</sup> and a monolayer graphene.<sup>31,32)</sup> We discuss its spin and magnetization and the probability weight of Bloch states constituting the wave packet in each of the RH and LH chain. We also carry out analyses based on the Green's functions in order to investigate the scattering at the CIF microscopically. All the following analysis is carried out at the temperature  $T = 0$  and we set  $\hbar = 1$  throughout this paper.

### 3.1 Time dependence of the observables

Let us first define the initial state  $|I\rangle$ : an electron with the spin  $\sigma_I$  is added at  $\mathbf{r}_{n_i,j_i}$  in the  $p_{\ell_i}$ -orbital to the ground state  $|F\rangle$  at  $t = 0$ , which reads as

$$|I\rangle \equiv \frac{1}{\sqrt{A}} \hat{p}_{n_i,j_i,\ell_i,\sigma_i}^\dagger |F\rangle, \quad (|F\rangle \equiv \prod_{m,\varepsilon_m \leq \varepsilon_F} \hat{c}_m^\dagger |0\rangle), \quad (7)$$

where  $|0\rangle$  is the vacuum,  $\varepsilon_F$  is the Fermi energy, and  $A$  is the normalization constant defined as  $A = \sum_{m,\varepsilon_m > \varepsilon_F} |T_{n_i,j_i,\ell_i,\sigma_i;m}|^2$ . In the Heisenberg picture, the  $t$  dependence of the expectation value of operator  $\hat{O}(\mathbf{r}_{n,j}, t) \equiv$

$\sum_{\ell, \ell', \sigma, \sigma'} \hat{P}_{n,j,\ell,\sigma}^\dagger(t)(O)_{p_{\ell,\sigma}, p_{\ell',\sigma'}} \hat{P}_{n,j,\ell',\sigma'}(t)$  can be calculated as

$$O(\mathbf{r}_{n,j}, t) \equiv \langle I, \sigma_I | \hat{O}(\mathbf{r}_{n,j}, t) | I, \sigma_I \rangle \\ = \sum_{\substack{m, m' \\ \ell, \ell', \sigma, \sigma'}} T_{n,j,\ell,\sigma;m}^*(O)_{p_{\ell,\sigma}, p_{\ell',\sigma'}} T_{n,j,\ell',\sigma';m'} e^{i(\varepsilon_m - \varepsilon_{m'})t} \langle \hat{c}_m^\dagger \hat{c}_{m'} \rangle_I, \quad (8)$$

where  $\langle \cdots \rangle_I \equiv \langle I | \cdots | I \rangle$  and we have used the relation Eq. (6) and  $\hat{c}_m^\dagger(t) = e^{i\varepsilon_m t} \hat{c}_m^\dagger$ . The expectation value of the spin  $S_\nu(\mathbf{r}_{n,j}, t)$  ( $\nu = x, y, z$ ) and the magnetization  $M_\nu(\mathbf{r}_{n,j}, t)$  can be obtained by replacing  $O$  with the spin matrix  $S_\nu$  or the magnetization matrix  $M_\nu = 2S_\nu + L_\nu$ . We note that the presence of the filled Fermi sea prevents the injected electrons from being scattered into the eigenstates with  $\varepsilon_m < \varepsilon_F$ . For one-particle description of wavepacket, such scattering processes are allowed at the interface.<sup>32)</sup> In this sense our formulation takes into account many-particle effects even in non-interacting systems.

### 3.2 The Bloch states constituting the wave packet

We now analyze the Bloch states  $|R(L); k, \mu\rangle$  constituting the wave packet scattered at the CIF. Although the wavenumbers are not good quantum numbers, we can project the eigenstate  $|m\rangle$  to the Bloch state  $|R(L); k, \mu\rangle$  with the wavenumber  $k$  and the band index  $\mu$  ( $= 1, 2, \dots, 18$ ) in the RH-only (LH-only) system. Here, we apply the periodic boundary condition (PBC) to obtain  $|R(L); k, \mu\rangle$  and the wavenumber  $k$  is a good quantum number in this system. Thus, we can obtain the weight of the Bloch states in the wave packet for any  $t$ . The Hamiltonian in the RH- or LH-only system under the PBC is diagonalized as

$$H_R = \sum_{k,\mu} E_{k,\mu}^R \hat{R}_{k,\mu}^\dagger \hat{R}_{k,\mu}, \quad H_L = \sum_{k,\mu} E_{k,\mu}^L \hat{L}_{k,\mu}^\dagger \hat{L}_{k,\mu}, \quad (9)$$

where  $E_{k,\mu}^R$  ( $E_{k,\mu}^L$ ) and  $\hat{R}_{k,\mu}^\dagger$  ( $\hat{L}_{k,\mu}^\dagger$ ) are the eigen energy and the creation operator of the Bloch state  $|R(L); k, \mu\rangle$ , respectively.  $\hat{R}_{k,\mu}^\dagger$  ( $\hat{L}_{k,\mu}^\dagger$ ) is defined as  $\hat{R}_{k,\mu}^\dagger$  ( $\hat{L}_{k,\mu}^\dagger$ )  $\equiv \sum_{n,i,\ell,\sigma} B_{i,\ell,\sigma;\mu}^{R(L)}$  ( $B_{i,\ell,\sigma;\mu}^{L(L)}$ )  $\hat{p}_{n,i,\ell,\sigma}^\dagger$ , where  $B_{i,\ell,\sigma;\mu}^{R(L)}$  ( $B_{i,\ell,\sigma;\mu}^{L(L)}$ ) ( $k$ ) is the  $18 \times 18$  matrix for each  $k$ , where the matrix elements are labeled by  $\{j, \ell, \sigma\}$  and  $\mu$ .

$\hat{c}_m^\dagger(t)$  in Eq. (5) can be represented by  $\hat{R}_{k,\mu}^\dagger(t)$  ( $\hat{L}_{k,\mu}^\dagger(t)$ ) as

$$\hat{c}_m^\dagger(t) = \sum_{k,\mu} [U_{k,\mu;m}^{R*} \hat{R}_{k,\mu}^\dagger(t) + U_{k,\mu;m}^{L*} \hat{L}_{k,\mu}^\dagger(t)], \quad (10)$$

where  $U_{k,\mu;m}^{R(L)*} = \langle R(L); k, \mu | m \rangle$ . This allows us to calculate the probability of finding the Bloch state  $|R(L); k, \mu\rangle$  in the RH (LH) chain  $w_{k,\mu}^R(t)$  [ $w_{k,\mu}^L(t)$ ] as

$$w_{k,\mu}^R(t) = \langle I | \hat{R}_{k,\mu}^\dagger(t) \hat{R}_{k,\mu}(t) | I \rangle, \quad w_{k,\mu}^L(t) = \langle I | \hat{L}_{k,\mu}^\dagger(t) \hat{L}_{k,\mu}(t) | I \rangle. \quad (11)$$

When the wave packet stays in the RH chain for small  $t$ , we obtain  $w_{k,\mu}^R(t) \neq 0$  for some  $|R; k, \mu\rangle$  with  $E_{k,\mu}^R \gtrsim \varepsilon_F$  and  $w_{k,\mu}^L(t) = 0$  for any  $|L; k, \mu\rangle$  with  $E_{k,\mu}^L \gtrsim \varepsilon_F$ . Here, we assume the initial position  $n_I$  is sufficiently far from the CIF and the approximate equality is due to the finite size effects. However, as soon as the wave packet enters the LH chain,  $w_{k,\mu}^L(t)$  also becomes finite for some  $|L; k, \mu\rangle$  with  $E_{k,\mu}^L \gtrsim \varepsilon_F$ , which reflects the scattering profile of the wave packet at the CIF. The bands with the energy  $E_{k,\mu}^{R(L)} \lesssim \varepsilon_F$  are assumed to be filled and do not change with  $t$ , which is valid at  $T = 0$ .

### 3.3 Scattering Green's function

As an alternative approach, we here consider one-electron scattering problems. The information of the microscopic one-electron processes is useful for the analysis of the scattering at the CIF discussed in Sec. 3.1. We calculate the probability of finding a Bloch state  $|L; k, \mu\rangle$  in the LH chain at  $t > 0$  with initial Bloch state  $|R; k', \mu'\rangle$  at  $t = 0$  in the RH chain. Since the wave packet considered in Sec. 3.1 consists of multiple Bloch states, information of the scattering of a specific Bloch state is important as their elementary information.

The electron is injected in the RH chain at initial time  $t = 0$  and then scattered at the CIF as discussed in Sec. 3.1. However, this time the injected electron is in the Bloch state  $|R; k', \mu'\rangle = \hat{R}_{k',\mu'}^\dagger |0\rangle$ . We denote the probability of finding the electron in the Bloch state  $|L; k, \mu\rangle = \hat{L}_{k,\mu}^\dagger |0\rangle$  in the LH chain for  $t > 0$  as  $|P_{k,\mu,k',\mu'}(t)|$ , where

$$P_{k,\mu,k',\mu'}(t) \equiv \langle F | \hat{L}_{k,\mu}(t) \hat{R}_{k',\mu'}^\dagger(0) | F \rangle \theta(t), \quad (12)$$

is a kind of retarded Green's function. Here,  $\theta(t)$  is the Heaviside's step function. Using Eq. (10) and the Fourier transformation, one obtains

$$P_{k,\mu,k',\mu'}(\omega) = \sum_{\varepsilon_m > \varepsilon_F} \frac{U_{k,\mu;m}^{L*} U_{k',\mu';m}^R}{\omega - \varepsilon_m + i\delta} \quad \text{with } 0 < \delta \ll 1. \quad (13)$$

Here,  $\omega$  is the frequency (energy).  $|P_{k,\mu,k',\mu'}(\omega)|^2$  gives the scattering probability of finding an electron with the wavenumber  $k$  and the energy  $\omega$  in the LH chain when the electron is injected to the RH chain with the wavenumber  $k'$  and the energy  $E_{k',\mu'}^R$ .

## 4. Results

In this section, we show our numerical results. To introduce the basic single-electron properties in the RH (LH) systems, we first discuss the dispersion of the single-handed chain  $E_{k,\mu}^{R(L)}$  in Eq. (9), the spin and the orbital angular momentum, and the magnetization of each band. Secondly, we demonstrate the time evolution of spin angular momentum and magnetization when an electron is injected in the RH chain at  $t = 0$  on the basis of Eq. (8). We also examine how the Bloch states forming the wave packets are scattered at the CIF. Then, we calculate the profile of  $|P_{k,\mu,k',\mu'}(\omega)|^2$  [Eq. (13)] and examine whether the CIF structure, i.e.,  $\phi$  dependence affects the profile of  $|P_{k,\mu,k',\mu'}(\omega)|^2$ . Lastly, we show the density of states (DOS) and the wave functions to analyze the spin-flip scattering in detail. Throughout this section, we set  $N = 50$ ,  $\lambda = 0.5$  and the filling  $n_f$  is  $n_f = 5$  per unit cell, which leads to  $\varepsilon_F \approx 1.01$ . Thus, we can focus on the upper six bands as enclosed by the dashed line in Fig. 2. We have checked that the results for  $N = 50$  is qualitatively unchanged even for larger system sizes up to  $N = 100$ .

### 4.1 Band dispersion

Figure 2 shows the band dispersion of the single-handed chain. The thick horizontal line represents the Fermi energy  $\varepsilon_F$ . The color represents the expectation value of the spin angular momentum  $S_{z,k,\mu}^{R(L)} \equiv \sum_{i=1,2,3} i \langle R(L); k, \mu | S_z | R(L); k, \mu \rangle_i$  [(a) and (d)], the orbital angular momentum  $L_{z,k,\mu}^{R(L)} \equiv \sum_{i=1,2,3} i \langle R(L); k, \mu | L_z | R(L); k, \mu \rangle_i$  [(b) and (e)], and the magnetization  $M_{z,k,\mu}^{R(L)} = L_{z,k,\mu}^{R(L)} + 2S_{z,k,\mu}^{R(L)}$  [(c) and (f)], where

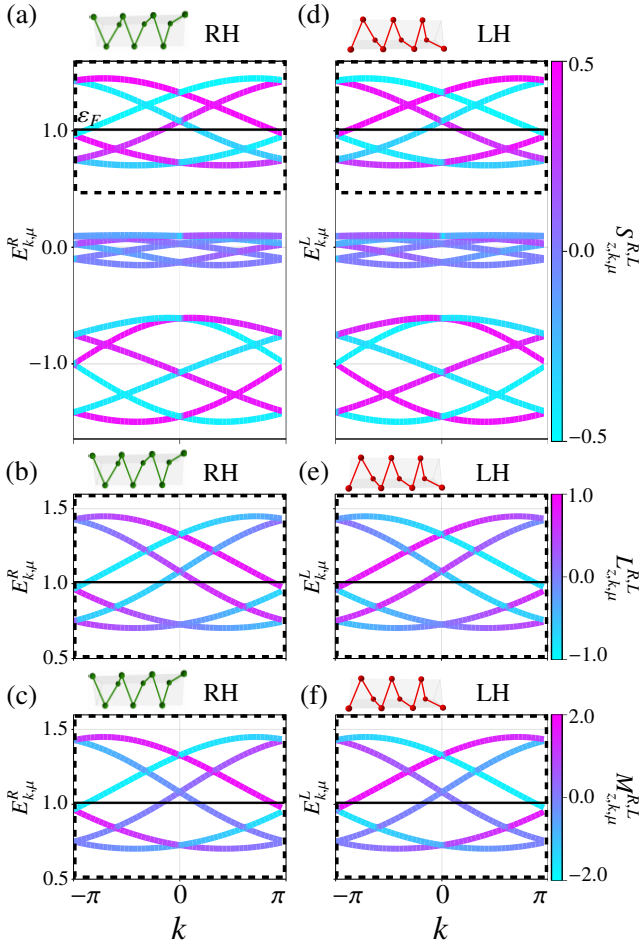


**Fig. 2.** Band dispersion of RH chain [(a)-(c)] and LH chain [(d)-(f)]. The color represents the expectation value of the spin angular momentum for the Bloch state  $S_{z,k,\mu}^{R(L)}$  in (a) and (d), the orbital angular momentum  $L_{z,k,\mu}^{R(L)}$  in (b) and (e) and magnetization  $M_z^{R(L)} = L_{z,k,\mu}^{R(L)} + 2S_{z,k,\mu}^{R(L)}$  in (c) and (f). For (b), (c), (e), and (f), the upper part of the dispersions enclosed by the dashed line in (a) and (d) is shown.

$|R(L); k, \mu\rangle_i$  is the  $i$ th sublattice component of the Bloch state. For Figs. 2(b), 2(c), 2(e), and 2(f), only the upper six bands are shown since the other bands below the Fermi energy are already filled and are not important in the analyses in the following. It is clear that the Bloch state  $|R(L); k, \mu\rangle$  is non degenerate owing to the high-symmetry or accidental points. Note that  $S_{z,k,\mu}^R = -S_{z,-k,\mu}^R = -S_{z,k,\mu}^L = S_{z,-k,\mu}^L$  and the similar relations hold for  $L_{z,k,\mu}^{R(L)}$  and  $M_z^{R(L)}$ . This is due to the time reversal symmetry and the lack of the  $z$  mirror symmetry.

#### 4.2 Time evolution of spin and magnetization

Figures 3 illustrates the time evolution of spin density  $S_z(\mathbf{r}_{n,j}, t)$  for (a)  $\phi = 0$  and (b)  $\phi = 2\pi/3$ , and that of  $M_z(\mathbf{r}_{n,j}, t)$  for (c)  $\phi = 0$  and (d)  $\phi = 2\pi/3$ . See Eq. (8). Here, the unit of time is  $\frac{1}{[\text{NN hopping in eV}]} \times 10^{-15}$  s. At  $t = 0$ , a spin up ( $\sigma_I = \uparrow$ ; red line) or down ( $\sigma_I = \downarrow$ ; blue line) electron is injected to the RH chain at  $(n_I, j_I, \ell_I) = (N - 6, 1, x)$ , which results in the nearly delta function-like peak at  $z_{N-6,1}$  at  $t = 0$ . This particular choice of initial state does not affect qualitatively the final results. We chose  $\ell_I = x$  since it creates clearer wave packet than  $\ell_I = y$  and  $\ell_I = z$  and thus it is useful for the

analyses. As the time evolves, the wave packet diffuses into a wave with positive group velocity ( $v^+$ -wave propagating in the positive  $z$  direction) and with negative group velocity ( $v^-$ -wave propagating in the negative  $z$  direction). Here, the Bloch states forming the  $v^+$ - and  $v^-$ -wave are indicated by the green and orange ovals, respectively in Figs. 3(e) and 3(i). We concentrate on the former in the following. When  $t \sim 60$ , the  $v^+$  wave reaches the CIF and the spin flip is observed for  $\phi = 0$ , while not for  $\phi = 2\pi/3$ .

Figures 3(e) and 3(f) show the  $k$ -resolved weight of the wave packets  $w_{k,\mu}^{R,L}(t)$  for  $\sigma_I = \downarrow$  [Eq. (11)] in the RH and LH chain, respectively for  $\phi = 0$ . Similarly, Figs. 3(g) and 3(h) show that for  $\phi = 2\pi/3$ . For  $\sigma_I = \uparrow$ , the corresponding  $k$ -resolved weights are shown in Figs. 3(i)–(l). For  $t \lesssim 60$ , the  $k$ -resolved weights are in the RH chain for the all cases, and thus the weights in the LH chain are zero [Figs. 3(f), 3(h), 3(j), and 3(l)]. For  $t \gtrsim 60$ , the  $v^+$ -wave enters the LH chain. One can notice that the Bloch states forming the  $v^+$ -wave in the LH chain remain the same branch in the  $k$ -space for  $\phi = 0$  [Figs. 3(f) and 3(j)], while they move toward “right” (“left”) for  $\sigma_I = \downarrow$  ( $\sigma_I = \uparrow$ ), i.e., the other branch with positive group velocity for  $\phi = 2\pi/3$  [Figs. 3(h) and 3(l)]. Thus, the wavenumber is approximately conserved after passing through the CIF for  $\phi = 0$ , while it is not for  $\phi = 2\pi/3$ . As shown in Figs. 2(a) and 2(b),  $S_{z,k,\mu}^R = -S_{z,k,\mu}^L$ , which means that the direction of the spin in the  $v^+$ -wave in the LH chain after the scattering at the CIF is flipped for  $\phi = 0$ . In contrast,  $S_{z,k,\mu}^L$  for the branch with the large weight in the LH chain in Figs. 3(h) and 3(l) is negative for  $\phi = 2\pi/3$ . This is consistent with the data that there is no spin flip for  $\phi = 2\pi/3$  in Fig. 3(b). As for the magnetization, we can carry out the similar argument. The quantitative difference is that some bands possess small  $|M_{z,k,\mu}^{R(L)}|$  as shown in Figs. 2(c) and 2(f). As a result, the wave packet with the negative magnetization almost vanishes in the LH chain for both  $\phi = 0$  [Fig. 3(c)] and  $\phi = 2\pi/3$  [Fig. 3(d)]. This suggests the CIF works as a magnetization filter prohibiting negative  $M_z$  inside the LH.

#### 4.3 The scattering probability of the single Bloch state

Let us now examine the scattering probability  $|P_{k,\mu,k^*,\mu^*}(\omega)|^2$  defined in Eq. (13). Here, we use  $k^*$  and  $\mu^*$  instead of  $k'$  and  $\mu'$  for the wavenumber and the band index of the initial state.

To address the correspondence between the following analysis and the results in Sec. 4.2, we choose the initial state with  $k^* = -\pi/2$  and  $\mu^* = 16$ . This is one of the Bloch states constituting the  $v^+$ -wave in the RH chain for  $\sigma_I = \downarrow$  [see Figs. 3(e) and 3(g)], which is colored in Fig. 4(a). The probability of finding an electron in  $|L; k, \mu\rangle$  is colored in Figs. 4(b)–4(d). For  $\phi = 0$  [Fig. 4(b)],  $|P_{k,\mu,k^*,\mu^*}(\omega)|^2$  is finite at  $k \approx k^*$  and  $\omega \approx E_{k^*,\mu^*}^R$ , where the spin and the magnetization are opposite in the RH and LH chain. This suggests that the spin flip occurs for  $\phi = 0$ , which is consistent with the result in Sec. 4.2. However, as  $\phi$  increases, a finite  $|P_{k,\mu,k^*,\mu^*}(\omega)|^2$  emerges at  $k \approx \tilde{k} > 0$  and  $\omega \approx E_{k^*,\mu^*}^R$ , i.e., the other band with the positive group velocity, where the sign of the spin is the same as the initial state. See Figs. 4(c) and 4(d). For  $\phi = 2\pi/3$  [Fig. 4(d)],  $|P_{k,\mu,k^*,\mu^*}(\omega)|^2$  at  $k \approx k^*$  almost vanishes and it is finite only in the other band at  $k \approx \tilde{k}$ , which implies that the spin does not flip for this case. From these results together with the previous ones in Sec. 4.2, we can conclude that the spin and the magnetization flip when the momentum and the energy are



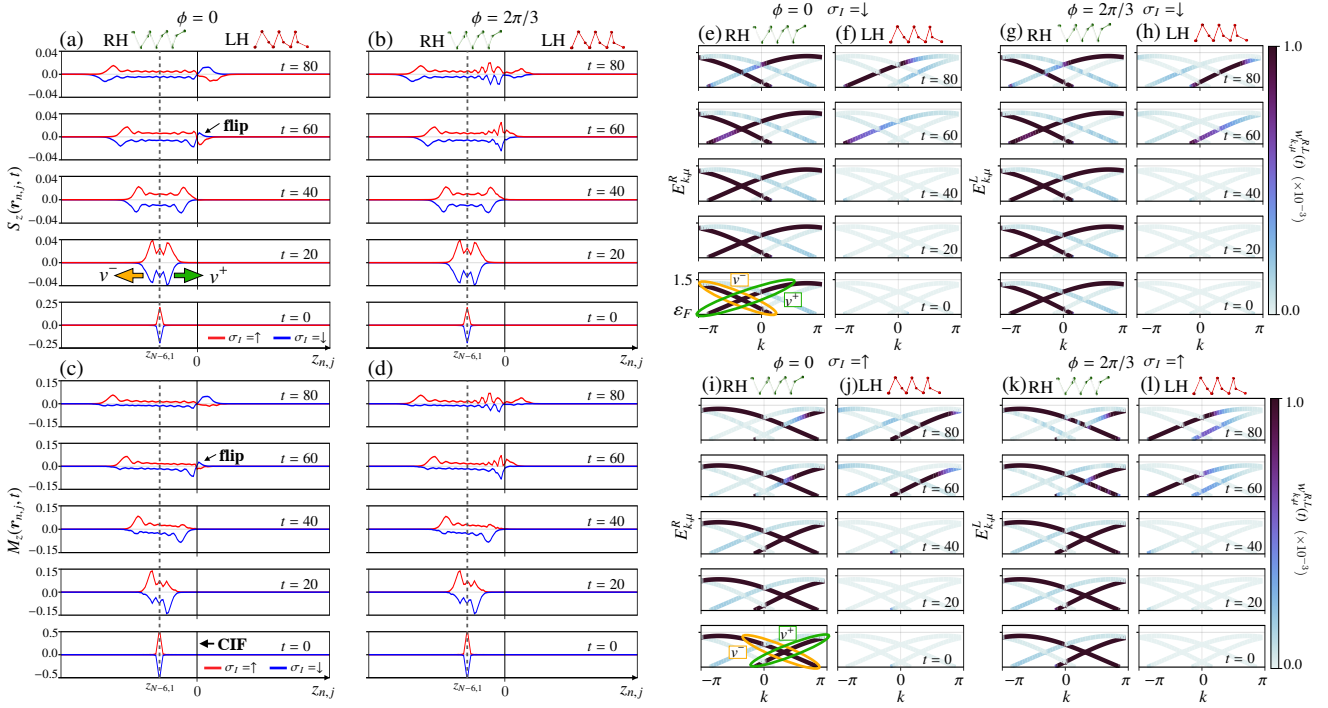


**Fig. 3.**  $S_z(r_{n,j}, t)$  with  $t = 0, 20, 40, 60,$  and  $80$  for (a)  $\phi = 0$  and (b)  $\phi = 2\pi/3$ , and  $M_z(r_{n,j}, t)$  for (c)  $\phi = 0$  and (d)  $\phi = 2\pi/3$ . The data for  $\sigma_I = \downarrow$  ( $\uparrow$ ) are colored in red (blue) and the initial position is indicated by the vertical dashed line. (e)-(l) The time evolution of the weight of the Bloch states constituting the wave packet  $w_{k,\mu}^{R(L)}(t)$  for  $\phi = 0$  and  $\sigma_I = \downarrow$  [(e) for RH and (f) for LH], for  $\phi = 2\pi/3$  and  $\sigma_I = \downarrow$  [(g) for RH and (h) for LH], for  $\phi = 0$  and  $\sigma_I = \uparrow$  [(i) for RH and (j) for LH], and for  $\phi = 2\pi/3$  and  $\sigma_I = \uparrow$  [(k) for RH and (l) for LH].

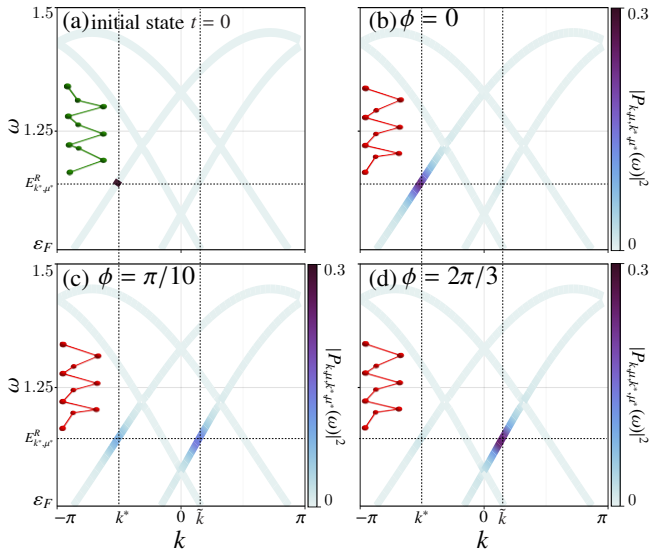


**Fig. 4.** The scattering probability  $|P_{k,\mu,k^*,\mu^*}(\omega)|^2$  for the initial state  $|R; k^*, \mu^*\rangle$ , where  $k^* = \pi/2$  and  $\mu^* = 16$ . (a) The initial state  $|R; k^*, \mu^*\rangle$ . Since this state is in the right-handed chain,  $S_z$  and  $M_z$  take negative values according to Figs. 2(a) and 2(c). (b)-(d)  $|P_{k,\mu,k^*,\mu^*}(\omega)|^2$  for (b)  $\phi = 0$ , (c)  $\phi = \pi/10$ , and (d)  $\phi = 2\pi/3$ .

approximately conserved during the scattering processes in this system.

#### 4.4 Density of states and localized modes

To discuss the relation between the electronic state and the spin-flip processes, we investigate the density of states (DOS), the local wave functions, and the number density at the CIF.

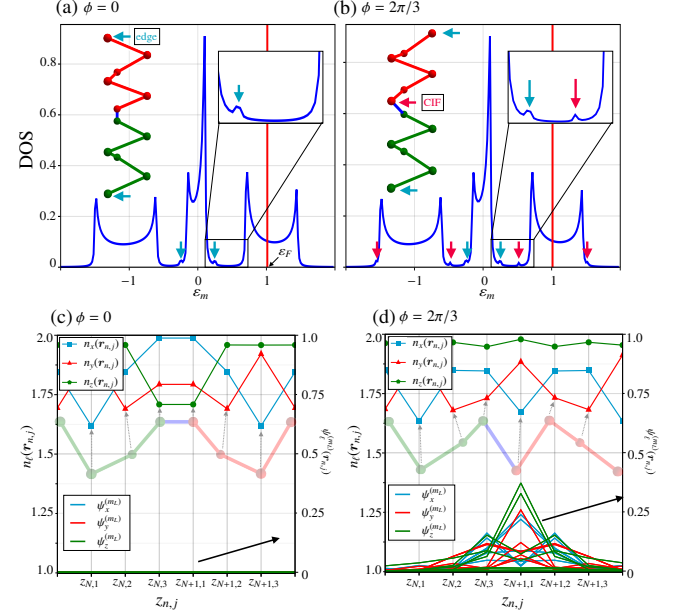


**Fig. 5.** DOS for (a)  $\phi = 0$  and (b)  $\phi = 2\pi/3$ . The red (sky blue) arrows indicate the localized state near the CIF (edges of chains). Corresponding positions are schematically shown. The insets show the zoom up near the energy where the localized states exist. (c) and (d) The number density of electrons in the  $p_\ell$  orbital  $n_\ell(r_{n,j})$  (left axis) and the amplitude of the wave function of the localized modes  $\psi_\ell^{(m_\ell)}(r_{n,j})$  (right axis).

Such localized states at interfaces have been observed along nematic domain walls in the scanning tunneling microscope measurement in FeSe<sup>33</sup>) and as explained below it is the key to the spin-flip mechanism in this system.

Figures 5(a) and 5(b) show the DOS for  $\phi = 0$  and  $\phi = 2\pi/3$ , respectively. Apart from three main separate parts, one can find spikes due to the localized modes as indicated by arrows. The blue arrows indicate the localized modes at the edges and the red ones do the localized modes at the CIF. The modes localized at the edges of the chain are found in both cases. However, the localized modes at the CIF are only found for  $\phi = 2\pi/3$ . Figures 5(c) and 5(d) show the number density  $n_\ell(\mathbf{r}_{n,j}) \equiv \sum_{\sigma=\uparrow,\downarrow} \langle F | \hat{p}_{n,j,\ell,\sigma}^\dagger \hat{p}_{n,j,\ell,\sigma} | F \rangle$  and the amplitude of the wave function of the localized modes  $m = m_L$ ,  $\psi_\ell^{(m_L)}(\mathbf{r}_{n,j}) \equiv \sum_{\sigma} \langle m_L | \hat{p}_{n,j,\ell,\sigma}^\dagger \hat{p}_{n,j,\ell,\sigma} | m_L \rangle$  for  $\phi = 0$  and  $\phi = 2\pi/3$ , respectively. This clearly shows there are localized modes at the CIF for  $\phi = 2\pi/3$  [Fig. 5(c)] and the  $p_z$  component  $\psi_z^{(m_L)}$  at the CIF is the largest among the three components followed by  $p_y$  and  $p_x$  orbital components. Thus, the number density of the  $p_z$  orbital  $n_z(\mathbf{r}_{n,i})$  is the largest among the three. In contrast, there are no localized modes for  $\phi = 0$  [Fig. 5(c)] and  $n_z(\mathbf{r}_{n,i})$  is the lowest.

## 5. Discussion

So far, we have demonstrated that the spin flip occurs for  $\phi = 0$ , where the localized modes at the CIF do not exist. In contrast, the spin does not flip when there are localized modes at the CIF for  $\phi = 2\pi/3$ . In the former case, the wavenumber of the electrons passing through the CIF is approximately the same, while in the latter, that is not conserved. For both cases, the energy is approximately conserved. In this section, we will discuss the mechanism of the spin flip at the CIF by analyzing the matrix elements of the SOC and  $\phi$  dependence of the total spin for the wave packet in the LH chain.

### 5.1 Mechanism of spin flip at the CIF

In our model [Eqs. (1) and (2)], the SOC accounts for the spin-flip scattering at the CIF. We first analyze the matrix elements of the SOC defined in Eq. (4) in detail. One of the  $2 \times 2$  off-diagonal block matrix between  $\{p_{x\uparrow}, p_{x\downarrow}\} \equiv \{p_x\}$  and  $\{p_{y\uparrow}, p_{y\downarrow}\} \equiv \{p_y\}$  has a form

$$\begin{pmatrix} i & 0 \\ 0 & -i \end{pmatrix}, \quad (14)$$

which is obviously diagonal in the spin index. However, the block matrices containing  $\{p_{z\uparrow}, p_{z\downarrow}\} \equiv \{p_z\}$  such as  $\{p_x\}$ - $\{p_z\}$  and  $\{p_y\}$ - $\{p_z\}$  are

$$\begin{pmatrix} 0 & 1 \\ -1 & 0 \end{pmatrix} \quad \text{and} \quad \begin{pmatrix} 0 & i \\ i & 0 \end{pmatrix}, \quad (15)$$

respectively. Note that they have off diagonal elements in the spin index. Thus, any spin-flip processes can occur only through the transitions to and from the  $p_z$  orbital.

Now, consider an electron which propagates in the RH chain for  $z < 0$  toward the CIF and hops from  $\mathbf{r}_{N,2}$  to  $\mathbf{r}_{N,3}$ . Figures 6(a) and 6(b) illustrate the schematic spin flip processes for  $\phi = 0$ . The incoming electron from  $\mathbf{r}_{N,2}$  hops to either the  $p_z$  or  $p_y$  orbital at  $\mathbf{r}_{N,3}$  because the bond  $\mathbf{d}_{2,3}^N$  between  $\mathbf{r}_{N,2}$  and  $\mathbf{r}_{N,3}$  only has the  $y$  and  $z$  components and the hopping is constrained to the  $\sigma$ -bond. Let us explain possible scattering processes with the spin flip in the first order in the SOC. When the electron hops to the  $p_z$  orbital at  $\mathbf{r}_{N,3}$  as shown in Fig. 6(a), it can directly hop to the  $p_z$  orbital at  $\mathbf{r}_{N+1,1}$  since the bond is along the  $z$  direction. Then, the electron hy-

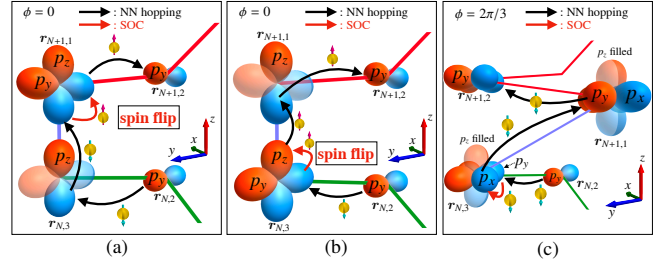


**Fig. 6.** Schematic pictures of spin-flip and no spin flip processes in the first order of  $\lambda$ . (a) The  $p_z$ -orbital electron at  $\mathbf{r}_{N,3}$  hops to the  $p_z$  orbital at  $\mathbf{r}_{N+1,1}$  and then the spin is flipped by the SOC for  $\phi = 0$ . (b) The  $p_y$ -orbital electron at  $\mathbf{r}_{N,2}$  hops to the  $p_y$  orbital at  $\mathbf{r}_{N,3}$ . The spin is flipped at the same site  $\mathbf{r}_{N,3}$  with the orbital changed into  $p_z$  via the SOC for  $\phi = 0$ . Then, the  $p_z$  electron can hop to the LH chain. (c) For  $\phi = 2\pi/3$ , the spin of  $p_y$  orbital electron is not flipped by the SOC since the  $p_z$  orbital is almost occupied. Thus, the SOC leads to the orbital flip from  $p_y$  to  $p_x$  without the spin flip. Then the  $p_x$  electron hops to the LH chain.

bridizes to the  $p_y$ -orbital with the spin flipped due to SOC and it hops to  $\mathbf{r}_{N+1,1}$ . In the case shown in Fig. 6(b), the electron in the  $p_y$ -orbital hybridize to the  $p_z$ -orbital through the SOC at  $\mathbf{r}_{N,3}$  and the spin is flipped and hops toward the LH chain for  $z > 0$ . In clear contrast, when  $\phi = 2\pi/3$ , the  $p_z$  orbital is almost occupied as shown in Fig. 5(d), where the  $p_z$  dominant localized modes at the CIF are the key to this. This suggests that the incoming electron cannot enter the  $p_z$  orbital at  $\mathbf{r}_{N,3}$  from  $\mathbf{r}_{N,2}$ . This also means that the  $p_y$  electron hops to either the  $p_x$  or  $p_y$  orbital at  $\mathbf{r}_{N+1,1}$ , since the  $p_z$  orbital is almost occupied at  $\mathbf{r}_{N+1,1}$ . During the hopping process above, one can consider the effects of the SOC. However,  $\{p_x\}$ - $\{p_y\}$  block of SOC is diagonal in the spin index, and thus, the spin is not flipped. These arguments qualitatively explain the numerical results in Sec. 4, which shows that the orbital degrees of freedom together with the SOC near the CIF play important role in the spin-flip scattering at the CIF.

### 5.2 $\phi$ dependence

So far, we have focused on the spin-flip processes in the two cases,  $\phi = 0$  and  $\phi = 2\pi/3$ . In order to check the validity of the analyses in Sec. 5.1, we examine the  $\phi$  dependence. We define the total  $S_z(\mathbf{r}_{n,i}, t)$  in the LH chain as  $S_z^L(t; \sigma_I) \equiv \sum_{n,i}^{N+1 \leq n \leq 2N} S_z(\mathbf{r}_{n,i}, t)$  with the initial spin  $\sigma_I$ . Figure 7(a) shows  $S_z^L(t; \sigma_I)$  for several values of  $\phi$  for  $\sigma_I = \downarrow$  (solid line) and  $\sigma_I = \uparrow$  (dashed line). For all  $\phi$ 's,  $S_z^L(t; \sigma_I) = 0$  for  $t \lesssim 50$  since the wave packet is in the RH chain. For  $t \gtrsim 50$ ,  $S_z^L(t; \sigma_I)$  is finite and becomes nearly constant at  $t \approx 300$ , which means that the wave packets no longer enter the LH chain.  $S_z^L(t; \downarrow) > 0$  and  $S_z^L(t; \uparrow) < 0$  indicates that the spin is flipped. Although the  $\phi$  dependence for the two cases  $\sigma_I = \uparrow$  and  $\downarrow$  are qualitatively similar when comparing  $S_z^L(t; \downarrow)$  and  $-S_z^L(t; \uparrow)$ , they are slightly different. Figure 7(b) shows  $\Delta S^L(t) \equiv S_z^L(t, \downarrow) + S_z^L(t, \uparrow)$ . As expected from the difference in the electronic states for  $\sigma_I = \uparrow$  and  $\downarrow$ ,  $\Delta S^L(t)$  is finite and the absolute value is approximately  $\sim 10\%$  of  $|S_z^L(t; \sigma_I)|$ . This suggests that a finite spin polarization is generated in the LH chain even when the injected electron is unpolarized and the polarization depends on the angle  $\phi$ . Note that  $|\Delta S_z^L(t)| > 0$  is in general the case but the results can be quantitatively modified when taking into account the interference between the

$\sigma_I = \uparrow$  and  $\downarrow$  wavepackets.

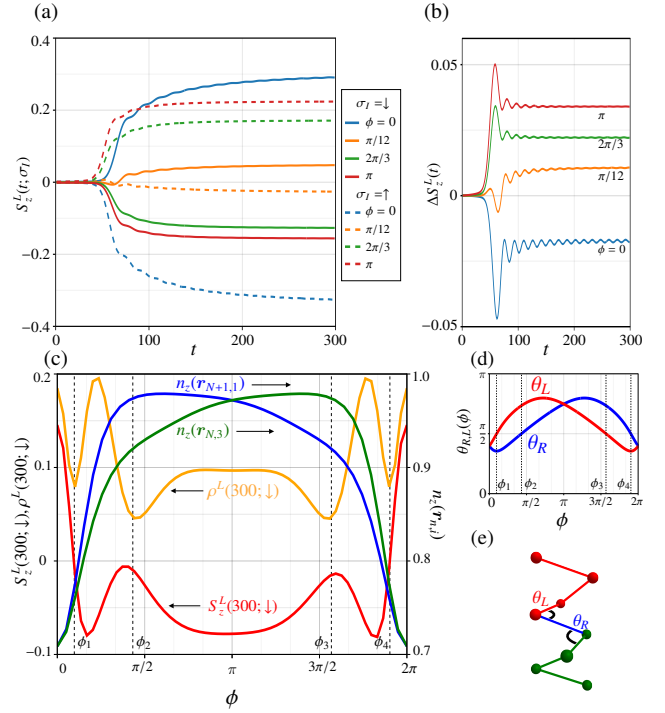
Now, we discuss the  $\sigma_I = \downarrow$  case in detail since qualitatively the same results are obtained for  $\sigma_I = \uparrow$ . In Fig. 7(c), we show the  $\phi$  dependence of  $S_z^L(300; \downarrow)$  and the total number of electrons in the LH chain  $\rho^L(t; \downarrow) \equiv \sum_{n,i}^{N+1 \leq n \leq 2N} \rho(\mathbf{r}_{n,i}, t)$ , where  $\rho(\mathbf{r}_{n,i}, t) = \langle I | \sum_{\ell, \sigma} \hat{p}_{n,i, \ell, \sigma}^\dagger(t) \hat{p}_{n,i, \ell, \sigma}(t) | I \rangle$ . As  $\phi$  increases,  $S_z^L(300; \downarrow)$  rapidly decreases and becomes negative, which means that the spin does not flip at the CIF. Meanwhile, the density of  $p_z$  electron at the CIF,  $n_z(\mathbf{r}_{N,3})$  and  $n_z(\mathbf{r}_{N+1,1})$  increase nearly as rapid as  $S_z^L(300; \downarrow)$  as shown by green and blue lines in Fig. 7(c). This evidences that the localized  $p_z$  electrons at the CIF prevent the incoming electrons from entering the  $p_z$  orbital and it suppresses the spin-flip scattering at the CIF. The increase in  $S_z^L$  for  $\phi \gtrsim \pi/6$ , which seems contradicting to our analyses in Sec. 4, is due to the reduction of the number of electrons entering the LH chain. Near the  $\phi$ 's where  $S_z^L$  takes the local maximum,  $\rho^L(300; \downarrow)$  does the local minimum as shown in Fig. 7(c). This means that there are fewer electrons in the LH chain and thus the absolute value of the spin decreases. There are also several  $\phi$ 's where  $\rho^L(300; \downarrow)$  takes the local minimum:  $\phi \approx \phi_1 = 0.097\pi$ ,  $\phi_2 = 0.432\pi$ ,  $\phi_3 = 1.568\pi$ ,  $\phi_4 = 1.903\pi$ . At these values of  $\phi$ 's, the inter-chain bond  $\mathbf{d}_{\text{CIF}}$  becomes orthogonal to either  $\mathbf{d}_{2,3}^N$  or  $\mathbf{d}_{1,2}^{N+1}$ , which leads to the reduction of  $\rho^L(300; \downarrow)$ .

Figure 7(d) shows the  $\phi$  dependence of the angle between  $\mathbf{d}_{\text{CIF}}$  and  $\mathbf{d}_{2,3}^N$ :  $\theta_R$  and that between  $\mathbf{d}_{\text{CIF}}$  and  $\mathbf{d}_{1,2}^{N+1}$ :  $\theta_L$ . See Fig. 7(e) for the schematic picture of the angles  $\theta_R$  and  $\theta_L$ . It is obvious that either  $\theta_R$  or  $\theta_L$  becomes  $\pi/2$  at  $\phi_\alpha$  ( $\alpha = 1, 2, 3, 4$ ). The  $\phi$  dependence  $\theta_{L,R}(\phi)$  is symmetric with respect to  $\phi = \pi$ , i.e.,  $\theta_R(\phi) = \theta_L(\phi + 2\pi)$ . It is natural that this interchange does not affect the number of electron in the LH chain at the sufficiently long time and thus  $\rho^L(300; \downarrow)$  is symmetric with respect to  $\phi = \pi$ . However, the orbital angular momentum of the electrons is not necessarily the same for  $\phi^*$  and  $-\phi^*$  and this also affects the spin angular momentum through the SOC. This is why  $S_z^L(300; \downarrow)$  is not symmetric with respect to  $\phi = \pi$  in Fig. 7(c).

The  $\phi$  dependence of  $S_z^L(t)$  clearly indicates the importance of the orbital profile of electronic states near the CIF as discussed in Sec. 5.1. This also means that the design of the interface between the two handedness can influence the spin transport properties through the CIF. In this study, the control parameter for the structure of the interface is only  $\phi$ . There are many other candidate parameters. For example, instead of directly connecting the two chains, one can introduce intermediate atoms between them and the electronic configuration of the atoms also affects the physics. Exploring such systems is an interesting problem and we leave the analyses about such setup as our future studies.

## 6. Conclusion

We have analyzed electronic states near the CIF and the spin transport through the CIF. Our model is a one-dimensional  $p$  electron model with the SOC and consisting of RH and LH chains connected at the CIF. We have carried out analyses of spin-polarized wave packet dynamics, one-electron scattering process, and the electronic states near the CIF. Our microscopic analysis reveals that the spin-flip scatterings at the CIF strongly depend on the local electronic states at the CIF. The geometrical aspects related to the orbital



**Fig. 7.** (a) Total spin angular momentum in the LH chain  $S_z^L(t; \sigma_I)$  for several  $\phi$ 's for the initial spin  $\sigma_I = \downarrow$  (solid line) and  $\sigma_I = \uparrow$  (dashed line). (b)  $\Delta S_z^L(t)$  for several  $\phi$ 's. (c)  $\phi$  dependence of  $S_z^L(t = 300; \downarrow)$  (red),  $\rho^L(t = 300; \downarrow)$  (orange),  $n_z(\mathbf{r}_{N,3})$  (green), and  $n_z(\mathbf{r}_{N+1,1})$  (blue). (d)  $\phi$  dependence of  $\theta_R$  (blue) and  $\theta_L$  (red). (e) Schematic picture of angles  $\theta_R$  and  $\theta_L$ .

profile of the localized states together with the spin-flip processes due to the SOC play an important role in determining whether the electron spin flips at the CIF or not. In particular, the key in our system is the  $p_z$  orbital at the CIF. This opens a way to manipulate the direction or polarization of the spin currents at the CIF by controlling the localized electron states without magnetic fields. For the deeper understanding and other mechanisms of the spin-flip processes in different systems further studies are needed and we leave them as our future problems.

## Acknowledgment(s)

The authors thank Takayuki Ishitobi, Takuya Nomoto, Takashi Hotta, and Hirokazu Kusunose for fruitful discussions. This work was supported by a Grant-in-Aid for Transformative Research Areas (A) ‘‘Asymmetric Quantum Matters’’, JSPS KAKENHI Grant Number JP23H04869.

- 1) W. Thomson, *Baltimore Lectures on Molecular Dynamics and the Wave Theory of Light* (C. J. Clay and Sons, London, 1904).
- 2) J. Kishine, H. Kusunose, and H. M. Yamamoto, *Isr. J. Chem.* **62**, e202200049 (2022).
- 3) S. Hayami and H. Kusunose, *J. Phys. Soc. Jpn.* **93**, 072001 (2024).
- 4) V. M. Edelstein, *Solid State Commun.* **73**, 233 (1990).
- 5) T. Furukawa, Y. Watanabe, N. Ogasawara, K. Kobayashi and T. Ito, *Phys. Rev. Res.* **3**, 023111 (2021).
- 6) R. Oiwa and H. Kusunose, *Phys. Rev. Lett.* **129**, 116401 (2022).
- 7) H. Zhu, J. Yi, M. Y. Li, J. Xiao, L. Zhang, C. W. Yang, R. A. Kaindl, L. J. Li, Y. Wang, and X. Zhang, *Science* **359**, 579 (2018).
- 8) M. Hamada, E. Minamitani, M. Hirayama, and S. Murakami, *Phys. Rev. Lett.* **121**, 175301 (2018).

- 9) K. Ishito, H. Mao, Y. Kousaka, Y. Togawa, S. Iwasaki, T. Zhang, S. Murakami, J.-i. Kishine, and T. Satoh, *Nat. Phys.* **19**, 35 (2022).
- 10) J. Kishine, A. S. Ovchinnikov, and A. A. Tereshchenko, *Phys. Rev. Lett.* **125**, 245302 (2020).
- 11) H. Tsunetsugu and H. Kusunose, *J. Phys. Soc. Jpn.* **92**, 023601 (2023).
- 12) L. Zhang and Q. Niu, *Phys. Rev. Lett.* **112**, 085503 (2014).
- 13) S. C. Guerreiro and S. M. Rezende, *Phys. Rev. B* **92**, 214437 (2015).
- 14) J. Holanda, D. S. Maior, A. Azevedo, and S. M. Rezende, *Nat. Phys.* **14**, 500 (2018).
- 15) F. Yang, M. Wang, D. Zhang, J. Yang, M. Zheng, and Y. Li, *Chem. Rev.* **120**, 2693 (2020).
- 16) U. K. Rössler, A. N. Bogdanov, and C. Pfeleiderer, *Nature* **442**, 797 (2006).
- 17) J. Ohe, T. Ohtsuki, and B. Kramer, *Phys. Rev. B* **75**, 245313 (2007).
- 18) S. Okumura, H. Ishizuka, Y. Kato, J. Ohe, and Y. Motome, *Appl. Phys. Lett.* **115**, 012401 (2019).
- 19) B. Göhler and V. Hamelbeck and T. Z. Markus and M. Kettner and G. F. Hanne and Z. Vager and R. Naaman and H. Zacharias, *Science* **331**, 894 (2011).
- 20) F. Evers, A. Aharony, N. Bar-Gill, O. Entin-Wohlman, P. Hedegård, O. Hod, P. Jelinek, G. Kamieniarz, M. Lemesko, K. Michaeli, V. Mujica, R. Naaman, Y. Paltiel, S. Refaely-Abramson, O. Tal, J. Thijssen, M. Thoss, J. M. van Ruitenbeek, L. Venkataraman, D. H. Waldeck, B. Yan, and L. Kronik, *Adv. Matter.* **34**, 2106629 (2022).
- 21) A. Inda, R. Oiwa, S. Hayami, H. M. Yamamoto, and H. Kusunose, *J. Chem. Phys.* **160**, 184117 (2024).
- 22) S. Hayami, R. Yambe, and H. Kusunose, *J. Phys. Soc. Jpn.* **93**, 043702 (2024).
- 23) Y. Togawa, Y. Kousaka, S. Nishihara, K. Inoue, J. Akimitsu, A. S. Ovchinnikov, and J. Kishine, *Phys. Rev. Lett.* **111**, 197204 (2013).
- 24) J. Kishine, I. V. Proskurin, and A. S. Ovchinnikov, *Phys. Rev. Lett.* **107**, 017205 (2011).
- 25) H. Watanabe, K. Hoshi, and J. Ohe, *Phys. Rev. B* **94**, 125143 (2016).
- 26) W. H. Butler, *Sci. Technol. Adv. Mater.* **9**, 014106 (2008).
- 27) J. C. R. Sánchez, and L. Vila, G. Desfonds, S. Gambarelli, J. P. Attané, J. M. D. Teresa, C. Magén, and A. Fert, *Nat. Commun.* **4**, 2944 (2013).
- 28) A. A. Tseng, *Small* **1**, 924 (2005).
- 29) J. C. Slater and G. F. Koster, *Phys. Rev.* **94**, 1498 (1954).
- 30) A. Chaves, G. A. Farias, F. M. Peeters, and B. Szafran, *Phys. Rev. B*, **80**, 125331 (2009).
- 31) G. M. Maksimova, V. Ya. Demikhovskii, and E. V. Frolova, *Phys. Rev. B* **78**, 235321 (2008).
- 32) A. Matulis, M. Ramezani Masir, and F. M. Peeters, *Phys. Rev. A* **86**, 022101 (2012).
- 33) Y. Yuan, W. Li, B. Liu, P. Deng, Z. Xu, X. Chen, C. Song, L. Wang, K. He, G. Xu, X. Ma, and Q.-K. Xue, *Nano Letters* **18**, 7176 (2018).